



Enhanced photodegradation of acetaminophen over Sr@TiO₂/UiO-66-NH₂ heterostructures under solar light irradiation

Y.L. Wang, M. Peñas-Garzón, J.J. Rodríguez, J. Bedia^{*}, C. Belver^{*}

Chemical Engineering Department, Universidad Autónoma de Madrid, Campus Cantoblanco, E-28049 Madrid, Spain

ARTICLE INFO

Keywords:

Sr@TiO₂/UiO-66-NH₂
Photocatalytic degradation
Acetaminophen
Continuous reaction
Solar light

ABSTRACT

Novel Sr@TiO₂/UiO-66-NH₂ heterostructures were synthesized by a two-step solvothermal approach and tested as photocatalysts for the solar degradation of acetaminophen. Strontium titanate was used as precursor to obtain the heterostructures, resulting in Sr@TiO₂ anchored and dispersed on the UiO-66-NH₂. The effect of the Sr@TiO₂/UiO-66-NH₂ ratio was analyzed. All the heterostructures were more active than the pattern UiO-66-NH₂, and the most active achieved more than 90% of conversion of acetaminophen. This enhanced degradation was ascribed to a better separation and faster transfer of charges, as confirmed by photoluminescence and electrochemical characterization. Radical trapping experiments revealed that superoxide radicals (O₂^{•-}) and to a lower extent photoinduced holes (h⁺) were involved in acetaminophen degradation. As a novelty, the activity and stability of the best photocatalyst were evaluated in a continuous flow reaction system, upgrading conventional short-cycle batch studies. The heterostructure maintained an almost constant high conversion of acetaminophen during the 10 h on stream of the experiment, demonstrating excellent photocatalytic performance and stability in water. Besides, the photocatalytic degradation intermediates were identified, and a corresponding pathway of ACE transformation was proposed.

1. Introduction

Pharmaceuticals and personal care products (PPCPs) include medicinal drugs for human and veterinary use, such as antibiotics, painkillers, antihypertensives, and anticancer drugs [1,2]. Among them, acetaminophen (ACE), also known as paracetamol, is the main ingredient in cold and flu medications to treat fever and relieve pain [3]. With the development of modern medical technology and the growth of the human population, the sales and use of medicinal drugs are continuously increasing. After ingestion by the human body and animals, only a fraction is metabolized, and the rest is excreted. Thus, medical drugs reach the municipal wastewater treatment plants (WWTPs), which are not designed to remove these compounds and, consequently, in most cases, they are present in the discharge streams. In addition, during their production process, PPCPs can be also discharged into the environment along with the industrial wastewater [4]. The PPCPs flowing into groundwater will be ecotoxic to microorganisms and plants and threaten the water environment. Therefore, the treatment of water containing PPCPs is of practical significance for environmental remediation.

Typically advanced oxidation processes (AOPs), such as Fenton,

sulfate (SO₄^{•-}) and photocatalytic oxidation, among others [5,6], can be used to remove contaminants. Photocatalysis is a light-driven clean-up technology using a semiconductor as photocatalyst with no need for additional reactants [7–9]. When the energy of light irradiation equals or exceeds the bandgap energy of the semiconductor, electrons (e⁻) can jump from the valence to the conduction band, generating holes (h⁺) in the former one. These h⁺ can react with H₂O/OH⁻ yielding hydroxyl radicals (•OH), while e⁻ can interact with O₂ generating superoxide radicals (O₂^{•-}), which can directly oxidize the organic contaminants in water to CO₂ and H₂O [10]. However, the main limitations of conventional photocatalysts are low light-harvesting and electron-hole recombination [11,12]. The literature reports a wide diversity of materials tested as photocatalysts for water treatment, with special attention to the use of solar light. Those materials include metal oxides [12–17], ternary compounds [18–20], sulfides [17,21,22], and more recently metal-organic frameworks (MOFs) [23–26]. MOFs are composed of metal clusters and multifunctional organic ligands connected by coordination bonds [27]. Their high porosity, tunable framework and semiconductor properties have increased the interest in their potential application in photocatalysis [28].

^{*} Corresponding authors.

E-mail addresses: jorge.bedia@uam.es (J. Bedia), carolina.belver@uam.es (C. Belver).

<https://doi.org/10.1016/j.cej.2022.137229>

Received 17 February 2022; Received in revised form 29 April 2022; Accepted 25 May 2022

Available online 27 May 2022

1385-8947/© 2022 The Author(s). Published by Elsevier B.V. This is an open access article under the CC BY-NC license (<http://creativecommons.org/licenses/by-nc/4.0/>).

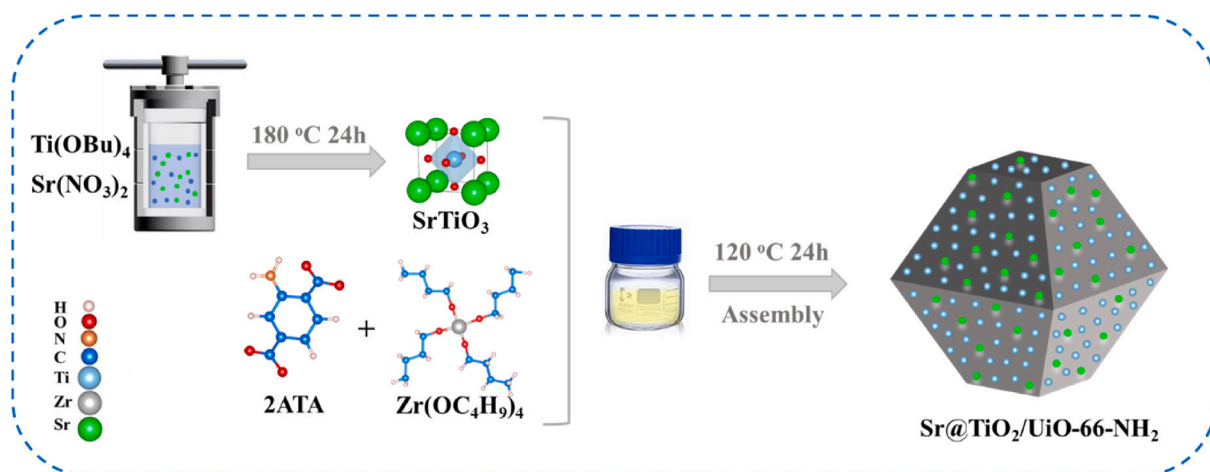


Fig. 1. Illustration of the synthesis of the Sr@TiO₂/UiO-66-NH₂ heterostructures.

In this sense, the photocatalytic performance of MOFs can be improved by different strategies, such as ligand functionalization, metal doping, nanoparticle decoration or constructing heterojunctions [23,29]. Our research group has widely analyzed the use of MOFs in solar photocatalytic treatment of water, with special attention to stable MIL-125 and UiO-66 MOFs [30–35]. The ligand functionalization with –NH₂ groups improves visible light absorption thus narrowing the bandgap of MOFs. The organic ligand is equivalent to a light-trapping antenna that can absorb photons giving rise to electrons and holes [36]. UiO-66-NH₂ consists of [Zr₆O₄(OH)₄] clusters interconnected by 2-amino terephthalic acid ligands. Due to the robust Zr–O interactions, this MOF displays excellent water and thermal stability [37]. The construction of heterojunctions is an alternative strategy for improving the light harvesting of photocatalysts. Heterojunctions are constructed by coupling two or more semiconductors and their behavior can be classified according to their band structure and the charge-transfer mechanism [38,39]. The combination of UiO-66-NH₂ with other semiconductors can result in a faster carrier transfer and a better hole-electron separation, thus enhancing the photocatalytic activity.

In this sense, TiO₂ can represent a suitable semiconductor to construct heterojunctions, due to the remarkable activity and stability of this well-known material [9,40]. However, the main limitations of TiO₂ are related to its wide bandgap value (3.2–3.3 eV), restricting the light absorption to the UV-region of the solar spectrum, and the high recombination rate of photogenerated charges, reducing the photocatalytic performance [41]. Different approaches have been previously reported to reduce the recombination rate (such as metal doping, dye-sensitization, or noble metal deposition), been usually used expensive noble or transition metals. Despite that, alkaline earth metals (such as Sr) decorating TiO₂ have been barely investigated to improve the performance of the semiconductor, mainly through the electron-trapping effect ascribed to the presence of these metals [42].

With the aim of enhancing the photocatalytic performance under solar light, novel Sr@TiO₂/UiO-66-NH₂ heterostructures were herein designed and prepared by a relatively simple two-step solvothermal method. The use of SrTiO₃ as precursor facilitates the preparation of the heterojunction including TiO₂ decorated with Sr, which can represent a suitable way to enhance the photocatalytic activity of the pristine MOF. To the best of our knowledge, this kind of heterojunction has not been reported before. A complete characterization was performed to establish the structure-performance relationships in the photocatalytic degradation of acetaminophen under simulated sunlight. Moreover, the radical species involved in the reaction were also explored by the corresponding charge trapping tests. As a novelty, the activity and stability of the best heterostructure were evaluated in a continuous flow experiment, replacing conventional but less informative short-cycle studies. To

reveal the photocatalytic mechanism, the intermediate products and transformation pathways were elucidated.

2. Experimental

2.1. Chemicals

Zirconium butoxide (Zr(OC₄H₉)₄, 80%), 2-aminoterephthalic acid (2ATA) (C₈H₇NO₄, 99%), Titanium(IV) butoxide (Ti(OBu)₄, ≥ 97%), formic acid (HCOOH, ≥ 95%), strontium nitrate (Sr(NO₃)₂, ≥ 99%), ethylene glycol (C₂H₆O₂, 95%), sodium hydroxide (NaOH, ≥ 97%), acetaminophen (ACE) (C₈H₉NO₂, ≥ 99%), methanol (CH₃OH, ≥ 99.9%), acetic acid (CH₃COOH, ≥ 99%), p-benzoquinone (p-BQ) (C₆H₄O₂, ≥ 98%), silver nitrate, (AgNO₃, ≥ 99%) and triethanolamine (C₆H₁₅NO₃, 98%) were all purchased from Sigma-Aldrich. N,N-dimethylformamide (C₃H₇NO, ≥ 99.8%) and 2-propanol (C₃H₈O, 99.7%) were acquired from Panreac. All these chemical reagents were of analytical grade and used without further purification.

2.2. Preparation of photocatalysts

2.2.1. Synthesis of SrTiO₃

SrTiO₃ was synthesized by a solvothermal method according to previous work [43]. Initially, Ti(OBu)₄ (5 mmol) and Sr(NO₃)₂ (5 mmol) were dissolved in ethylene glycol (60 mL) by stirring for 10 min. Then, 1.5 M NaOH (15 mL) was carefully added dropwise to the above solution. After stirring for 10 min, the suspension was transferred and sealed in the Teflon-lined autoclave for solvothermal treatment at 180 °C for 24 h. The obtained products were purified with deionized water and dried overnight at 70 °C.

2.2.2. Synthesis of UiO-66-NH₂

The UiO-66-NH₂ was prepared via a solvothermal method following previous work [34]. Briefly, Zr(OC₄H₉)₄ (1.5 mmol), 2ATA (1.5 mmol) and formic acid (10 mL) were mixed into DMF solution (20 mL) in a 100 mL Schott bottle. The resulting suspension was sonicated until obtaining a homogeneous solution and then subjected to thermal heating at 120 °C for 24 h. The resulting samples were washed with DMF and methanol several times and further vacuum-dried at 70 °C for 12 h.

2.2.3. Synthesis of Sr@TiO₂ and Sr@TiO₂/UiO-66-NH₂ heterostructures

Sr@TiO₂/UiO-66-NH₂ heterostructures were synthesized using the as-prepared SrTiO₃ as a sacrificial precursor and growing the UiO-66-NH₂ on it. For this purpose, a specific amount of SrTiO₃ was introduced in the aforementioned UiO-66-NH₂ synthesis, following the same procedure and washing steps. Three different heterostructures were

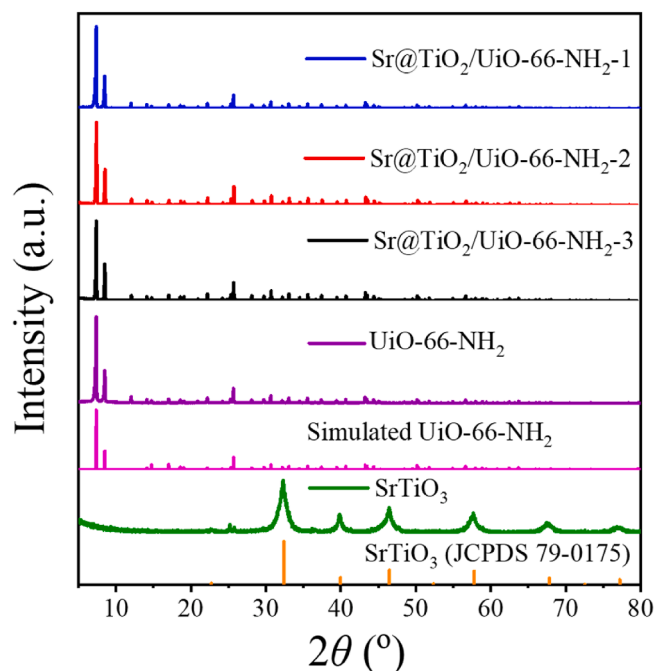


Fig. 2. XRD patterns of bare semiconductors and synthesized heterostructures.

prepared depending on the SrTiO_3 amount used, 0.75, 1.5 or 3.0 mmol, referred as $\text{Sr@TiO}_2/\text{Uio-66-NH}_2\text{-1}$, $\text{Sr@TiO}_2/\text{Uio-66-NH}_2\text{-2}$ and $\text{Sr@TiO}_2/\text{Uio-66-NH}_2\text{-3}$, respectively. To investigate the transformation of SrTiO_3 during the solvothermal synthesis of the heterostructures, comparative experiments were designed. (i) A certain mass of as-prepared SrTiO_3 was dispersed in 20 mL DMF, sealed in a Schott bottle, and heat-treated at 120 °C for 24 h. The washing process is identical to that of Uio-66-NH_2 . This sample was referred to as $\text{SrTiO}_3\text{-DMF}$. (ii) Sr@TiO_2 sample was prepared by the same process as $\text{Sr@TiO}_2/\text{Uio-66-NH}_2$, except that the 2ATA linker and $\text{Zr(OC}_4\text{H}_9)_4$ were not added. The whole process of preparing these heterostructures is schematized in Fig. 1. Based on the following discussion of the results, it can be rationalized that during the synthesis process, SrTiO_3 was converted to Sr@TiO_2 and combined with the Uio-66-NH_2 framework.

2.3. Characterization of materials

X-ray diffraction (XRD) patterns were recorded in the range of $2\theta = 5\text{--}80^\circ$ with a scan rate of $1.5^\circ \text{ min}^{-1}$ using a Bruker D8 diffractometer with a $\text{Cu-K}\alpha$ ($\lambda = 0.15406 \text{ nm}$) radiation source. The crystal size was determined by Scherrer's equation from the most intense peak. The porous texture of the samples was characterized by N_2 adsorption-desorption at -196°C using a micromeritics TriStar 123 apparatus. The specific surface area (S_{BET}) was calculated by the Brunauer-Emmett-Teller (BET) equation [44]. The microporous volume (V_{MP}) and external or non-microporous surface area (S_{EXT}) were determined by the t-plot method [45]. The total pore volume (V_{p}) was evaluated from the amount of nitrogen (as liquid) adsorbed at $P/P_0 = 0.99$, where P and P_0 denote the equilibrium and saturation pressure of nitrogen at -196°C , respectively. Before measurement, all samples were outgassed overnight at 120 °C under vacuum. The UV-visible diffuse reflectance spectra (UV-vis-DRS) of the synthesized materials were recorded with a Japan Shimadzu 2600 UV-vis spectrophotometer using BaSO_4 as a reference in the wavelength range of 200–800 nm. Tauc plots were used to estimate the band gap energy of the prepared samples, assuming that all of them were indirect semiconductors [34]. Scanning electron microscopy SEM (Quanta 3D FEG, FEI) and transmission electron microscopy (TEM, Talos F200X, FEI, USA) complement the materials characterization. A benchtop total reflection X-ray fluorescence (TXRF) photometer

(Picofox™ S2, Bruker, Karlsruhe, Germany) was used to determine Zr, Ti and Sr concentrations. X-ray Photoelectron Spectroscopy (XPS) was performed with a Thermo Scientific apparatus using $\text{Al K}\alpha$ radiation (1486.68 eV). All XPS spectra were corrected using the binding energy of C–C at 284.6 eV. The binding energy was obtained in the 0 to 1200 eV range. Photoluminescence (PL) spectra were recorded at room temperature using an excitation wavelength of 310 nm and using a Varian Cary Eclipse fluorescence spectrophotometer. Time Resolved Fluorescence (TRF) spectra were recorded by an FL920 fluorescence spectrometer (Edinburgh Instruments Ltd) equipped with a 450 W xenon lamp. Mott-Schottky and electrochemical impedance spectroscopy (EIS) measurements were performed in a Metrohm Autolab PGSTAT204 electrochemical workstation. The sample suspension ($1 \text{ mg}\cdot\text{mL}^{-1}$) was prepared in 0.1 M Na_2SO_4 and placed into the electrochemical cell (DropSens ITO10). The Mott-Schottky plot measurements were recorded at 1000 Hz. The flat band potential of the materials, V_{fb} , was obtained following Mott-Schottky equation [46]:

$$\frac{1}{C^2} = \frac{2}{\epsilon \cdot \epsilon_0 \cdot e \cdot N_{\text{D}}} \left(V - V_{\text{fb}} - \frac{k \cdot T}{e} \right) \xrightarrow{1/C^2=0} V_{\text{fb}} = V - \frac{k \cdot T}{e}$$

being C the capacitance of the semiconductor-electrolyte junction at applied voltage V ; ϵ and ϵ_0 the permittivity of the semiconductor and the void, respectively; e the electron charge ($1.602 \cdot 10^{-19} \text{ J}$); k the Boltzmann's constant ($8.617 \cdot 10^{-5} \text{ eV}\cdot\text{K}^{-1}$) and T the temperature (298 K). V_{fb} is estimated from the intercept point of the tangent line with the potential axis ($1/C^2 = 0$) in the plot of $1/C^2$ vs V .

2.4. Photocatalytic degradation tests

The photocatalytic performance of the synthesized heterostructures was assessed by the photodegradation of acetaminophen (ACE) in water under solar light. A solar simulator equipped with a Xe lamp ($600 \text{ W}\cdot\text{m}^{-2}$, Suntest XLS+, ATLAS) and a 320 nm cut-off filter was used for the tests. The photocatalyst ($250 \text{ mg}\cdot\text{L}^{-1}$) was suspended in a 150 mL solution of ACE (initial concentration = $5 \text{ mg}\cdot\text{L}^{-1}$) and kept under stirring for 60 min in dark to reach adsorption equilibrium. Further, the light was switched on and aqueous samples (0.45 mL) were taken at specific time intervals and filtered with a PTFE syringeless filter (Whatman 0.2 μm). The ACE concentration was followed through high-performance liquid chromatography (HPLC, Shimadzu Prominence-I LC-2030C) with a diode array detector (SPDM30 A) and a C18 column (Eclipse Plus 5 μm , Agilent). The chromatographic method used a gradient mobile phase, including two mobile phases of 0.1% acetic acid aqueous solution and acetonitrile at a flow rate of $0.7 \text{ mL}\cdot\text{min}^{-1}$. Quantification of short-chain carboxylic acids was performed with a Kinetex XB-C18 column. Mobile phases consisted of 0.1% H_3PO_4 and H_2O at a flow rate of $0.5 \text{ mL}\cdot\text{min}^{-1}$ and a temperature of 30°C . The reaction intermediates were identified by liquid chromatography and electrospray ionization-mass spectrometry (LC/ESI-MS) technique. Mass spectra were acquired in positive electrospray ionization (ESI) mode in a scan range from 50 to 3000 m/z at a dry gas flow of $8.0 \text{ L}\cdot\text{min}^{-1}$ at 300°C , a capillary voltage of +3,500 V, and endplate offset voltage of 500 V. The total organic carbon (TOC) was determined using a Shimadzu TOC-L analyser. The experiments were performed in duplicates with standard deviations below 5%, indicated by error bars. The corresponding pseudo-first-order rate constants (k) are displayed as average values.

The ACE degradation was also studied in a continuous flow system (Fig. S1). The inlet channel and outlet channel were added to the original reactor. Two peristaltic pumps were used at the entry and exit to make the liquid flow continuously at $0.7 \text{ mL}\cdot\text{min}^{-1}$ to keep the catalyst concentration in the reactor constant ($250 \text{ mg}\cdot\text{L}^{-1}$). A filter device was incorporated at the sample outlet avoiding catalyst loss with the exit stream.

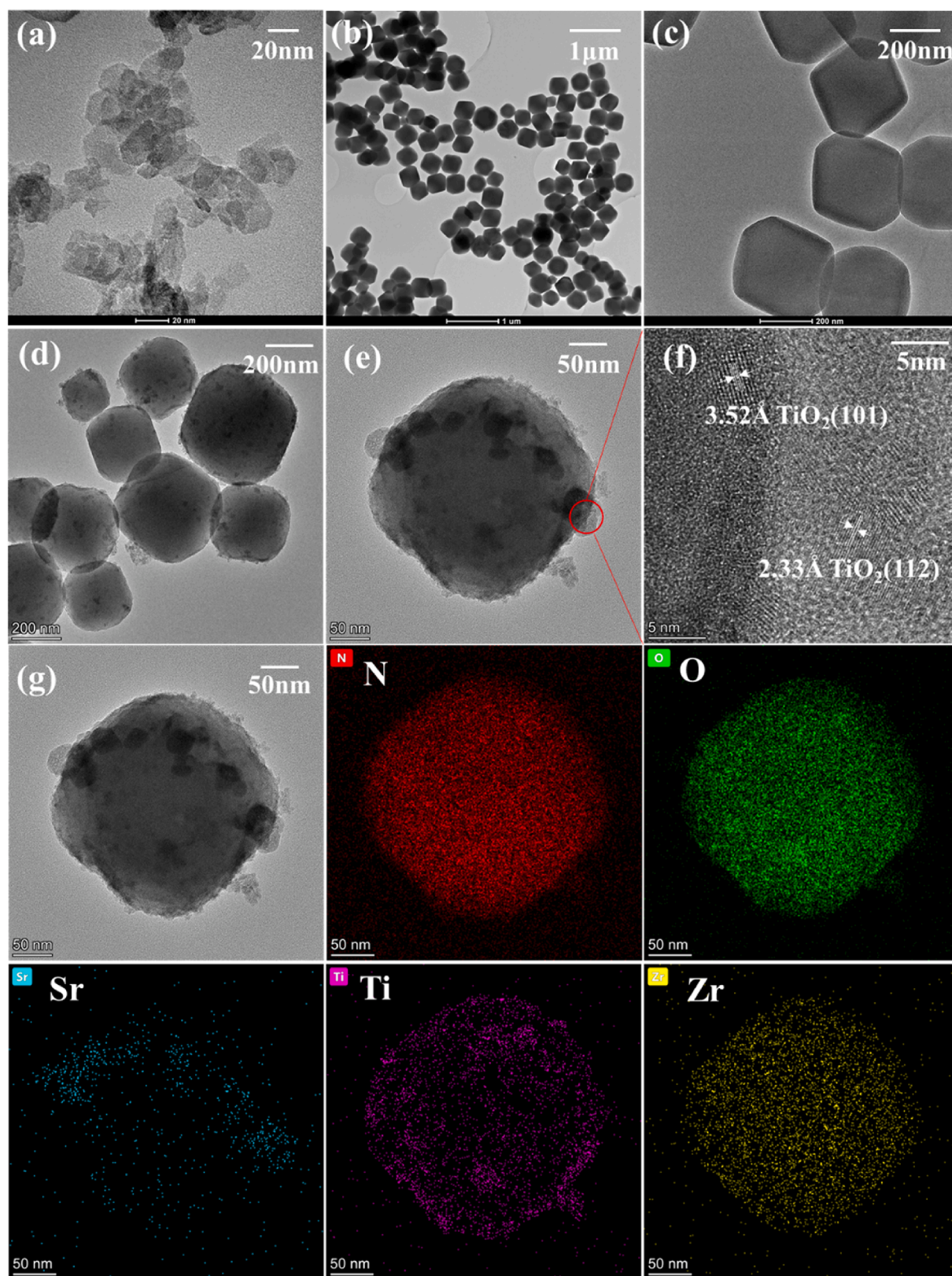


Fig. 3. TEM of (a) SrTiO₃, (b)(c) pristine UiO-66-NH₂, (d)(e) Sr@TiO₂/UiO-66-NH₂-2, (f) HRTEM image of Sr@TiO₂/UiO-66-NH₂-2 and (g) EDS mapping of N, O, Sr, Ti and Zr elements in Sr@TiO₂/UiO-66-NH₂-2.

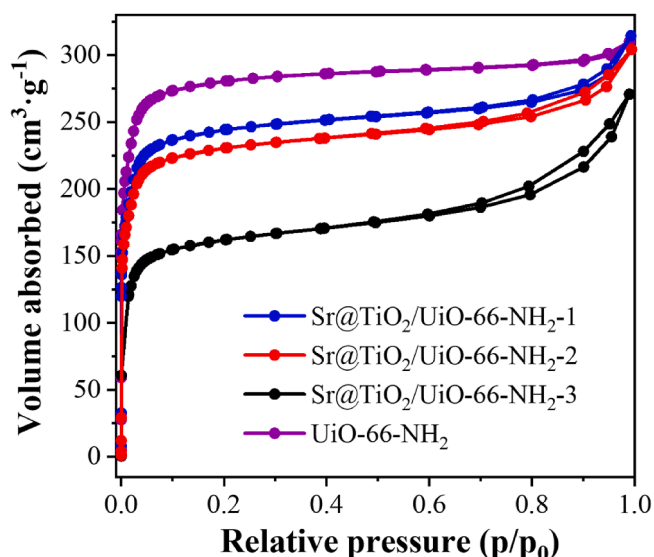


Fig. 4. N_2 adsorption-desorption isotherms at -196°C .

Table 1

Porous texture parameters and bandgap values.

Sample	S_{BET} (m^2/g)	S_{EXT} (m^2/g)	V_{MP} (cm^3/g)	V_{T} (cm^3/g)	Bandgap (eV)
Uio-66-NH ₂	910	34	0.42	0.48	2.85
Sr@TiO ₂ /Uio-66-NH ₂ -1	794	135	0.32	0.49	2.82
Sr@TiO ₂ /Uio-66-NH ₂ -2	750	133	0.30	0.47	2.80
Sr@TiO ₂ /Uio-66-NH ₂ -3	532	138	0.19	0.42	2.82

Note: S_{BET} —specific surface area, S_{EXT} —external or non-microporous surface area, V_{MP} —microporous volume, V_{T} —total pore volume.

3. Result and discussion

3.1. Characterization

The SrTiO_3 precursor was successfully prepared by solvothermal synthesis as revealed the diffraction peaks observed in the XRD diffractogram (Fig. 2), corresponding to the JCPDS 79-0175 pattern [43]. The Uio-66-NH₂ shows the characteristic reflections of this MOF (CCDC 1405751) with sharp peaks at 7.4 and 8.5° indicative of the high crystallinity of this sample [47,48]. All heterojunctions depict diffractograms similar to that of the pristine Uio-66-NH₂, suggesting that the

combined synthesis does not affect the structural integrity of the MOF. No additional peaks coming from the SrTiO_3 precursor were observed in the diffractograms, which can be ascribed to the lower crystallinity or the transformation of SrTiO_3 during the MOF synthesis. In Fig. S2, the transformation of SrTiO_3 was explored. The results showed that DMF did not have a significant effect on SrTiO_3 , since the XRD patterns of SrTiO_3 -DMF and SrTiO_3 were the same. However, the addition of formic acid decomposes SrTiO_3 into Sr and TiO_2 . The diffraction peaks of Sr@TiO_2 match well with the TiO_2 anatase phase (JCPDS 21-1272), clearly differing from the SrTiO_3 pattern. This is probably because the Sr-O bond in SrTiO_3 is broken by the corrosive nature of formic acid [49], resulting in the formation of a more stable TiO_2 . The analysis of the crystal size (Table S1) shows a slight increase in the MOF crystal size with the increase in the amount of SrTiO_3 used in the synthesis.

SrTiO_3 shows a layered morphology with an irregular shape (Fig. 3a and Fig. S3a of supplementary information), which contrasts with the decahedral morphology of Uio-66-NH₂ (Fig. 3b-c) that has an average particle size of c.a. 280 nm, very similar to the values reported in the literature [50]. The heterojunctions maintain the decahedral shape of the MOF but with a rougher surface when combined with different amounts of the precursor SrTiO_3 (Fig. S3d-e). Fig. 3d-e show in more detail the surface of $\text{Sr@TiO}_2/\text{Uio-66-NH}_2$ -2 covered with globular particles. These particles show an average size of 30 nm (Fig. 3e-f) and lattice-spacings of 3.52 and 2.33 Å, which correspond well to the (101) and (112) planes of TiO_2 anatase, respectively (JCPDS 21-1272). It should be noted the absence of crystals with the characteristic lattice space of SrTiO_3 (3.90 Å), which would indicate the transformation of the precursor during the second solvothermal synthesis step. The presence and distribution of the main elements in $\text{Sr@TiO}_2/\text{Uio-66-NH}_2$ -2 can be seen in the EDS mapping analysis (Fig. 3g). Zr, O, and N, as the main elements of MOF, are all homogeneously distributed in the particle. In contrast, Ti appears localized in the globular particles most likely in form of anatase TiO_2 . It is also worth noting the presence of Sr, although to a lesser extent than Ti, which is unevenly distributed. The Zr, Ti and Sr concentrations in the three heterostructures were determined by TXRF (Table S1). The Zr/Ti molar ratio was controlled by varying the SrTiO_3 amount added during the synthesis, while the Sr/Ti molar ratio remains almost constant. It should be noted that these Sr/Ti molar ratios of the heterostructures (ca., 0.2–0.3) are significantly lower than that of the pattern SrTiO_3 . This supports that during the synthesis the SrTiO_3 added is transformed into Sr@TiO_2 (in agreement with the observed lattice spaces) probably due to the acidic medium caused by the addition of formic acid.

N_2 adsorption-desorption isotherms and porous texture parameters of all synthesized materials are displayed in Fig. 4 and Table 1, respectively. Uio-66-NH₂ depicts a type I isotherm characteristic of solids with a well-developed microporosity. When the Uio-66-NH₂ is combined with Sr@TiO_2 , the resulting $\text{Sr@TiO}_2/\text{Uio-66-NH}_2$

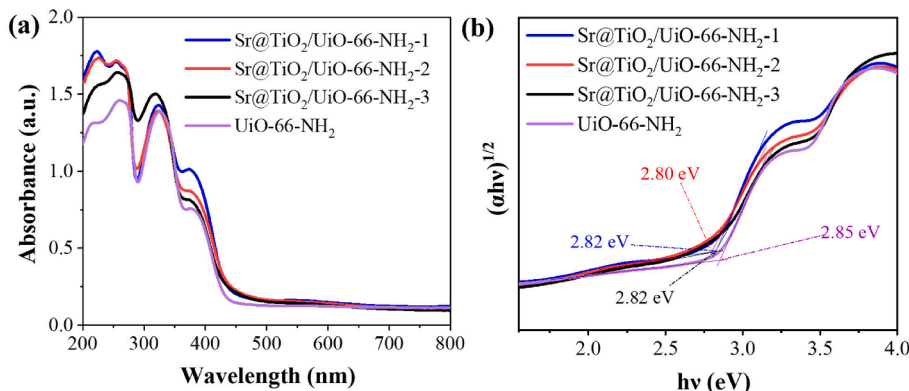


Fig. 5. (a) UV-vis DRS spectra and (b) Tauc plots of $(\alpha h\nu)^{1/2}$ vs. photon energy of synthesized materials.

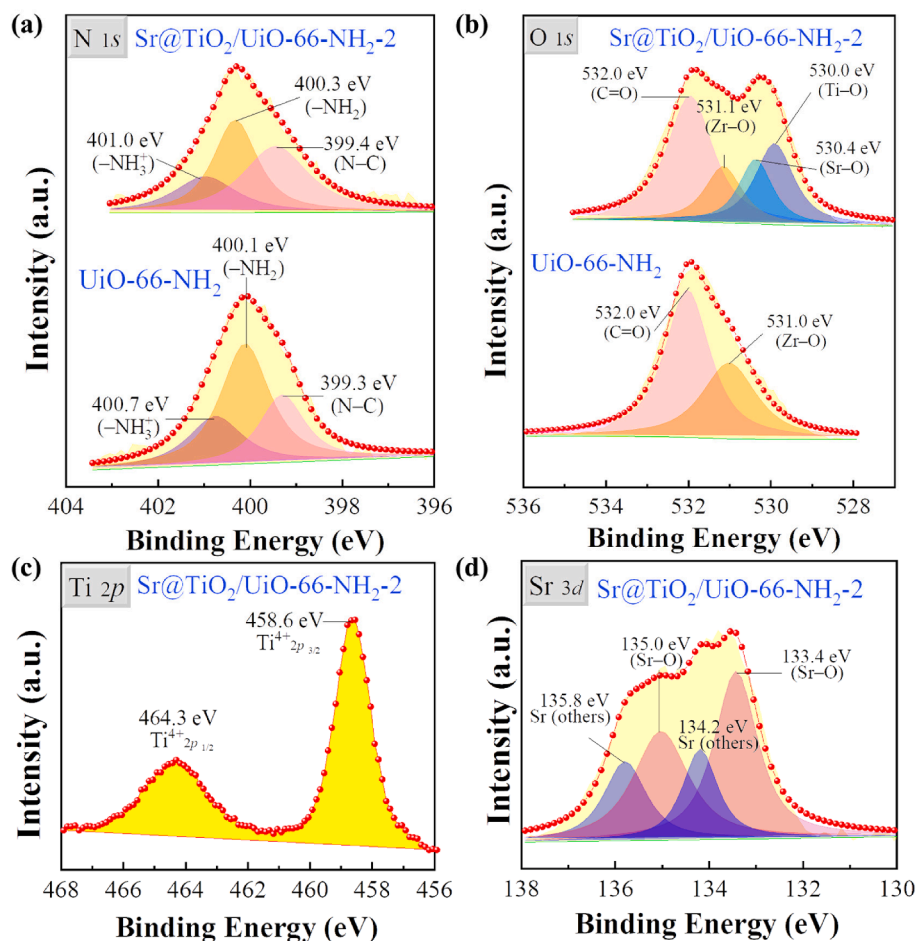


Fig. 6. High-resolution XPS spectra of (a) N 1s and (b) O 1s of UiO-66-NH₂ and Sr@TiO₂/UiO-66-NH₂-2, and (c) Ti 2p and (d) Sr 3d of Sr@TiO₂/UiO-66-NH₂-2.

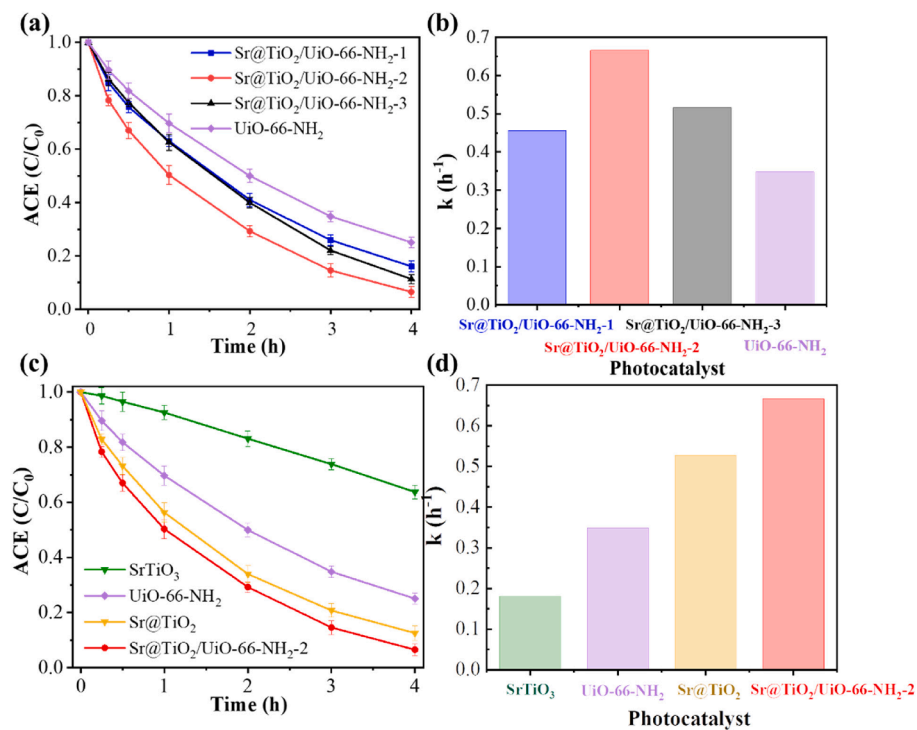


Fig. 7. (a) and (c) Evolution of ACE with the irradiation time and (b) and (d) pseudo-first-order rate constants (k , R^2 greater than 0.99) with all synthesized materials ([ACE]₀ = 5 mg·L⁻¹; [catalyst] = 250 mg·L⁻¹; Intensity = 600 W·m⁻²).

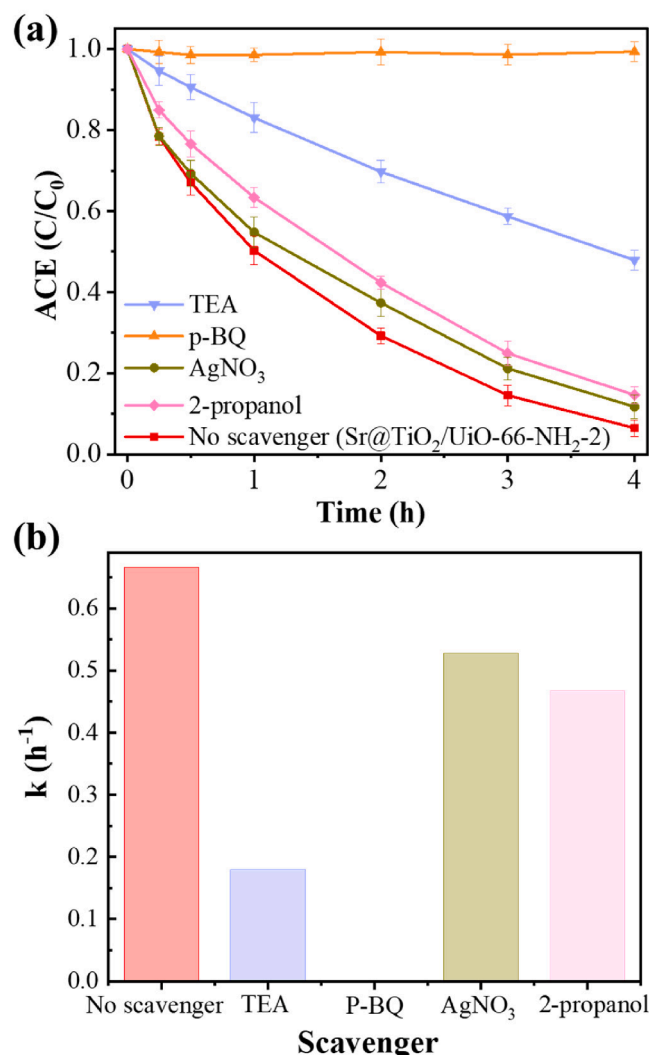


Fig. 8. (a) ACE evolution and (b) pseudo-first-order rate constants (k) with different scavengers for Sr@TiO₂/UiO-66-NH₂-2 ([ACE]₀ = 5 mg·L⁻¹; [scavenger] = 1 mM; Intensity = 600 W·m⁻²).

heterojunctions show also type I isotherms similar to that of the pattern MOF, which changes to a combination of type I and II when the amount of Sr@TiO₂ increases. The surface area and micropore area values of the Sr@TiO₂/UiO-66-NH₂ heterojunctions decrease with increasing Sr@TiO₂, most likely due to partial blockage of the MOF microporosity.

Fig. 5a compares the UV-vis DRS spectra of the synthesized materials. All heterostructures describe similar spectra to that of UiO-66-NH₂. The bands below 280 nm are ascribed to the electron transfer between O and Zr centres in the [Zr₆O₄(OH)₄] metal cluster, while the peaks above 310 nm are associated with the absorption in amine ligand groups and the ligand-to-metal charge transfer [51,52]. No significant absorption contribution from Sr@TiO₂ was observed. Band gap values (Table 1) were determined from these spectra by the Tauc's plot (Fig. 5b). All heterostructures have bandgap values very similar to that of UiO-66-NH₂, indicating that the light absorption of these heterostructures is due to the MOF presence, with no or little effect of the Sr@TiO₂.

XPS was applied to examine the near-surface region chemical composition and oxidation states of existing elements of UiO-66-NH₂ and Sr@TiO₂/UiO-66-NH₂-2. The XPS survey spectra (Fig. S4a) confirm the existence of C, O, N and Zr elements in UiO-66-NH₂, and that of Sr and Ti in Sr@TiO₂/UiO-66-NH₂-2 heterostructure. The C 1s and Zr 3d spectra of Sr@TiO₂/UiO-66-NH₂-2 and UiO-66-NH₂ are very similar (Fig. S4b,c), with the characteristic peaks of the MOF without changes in

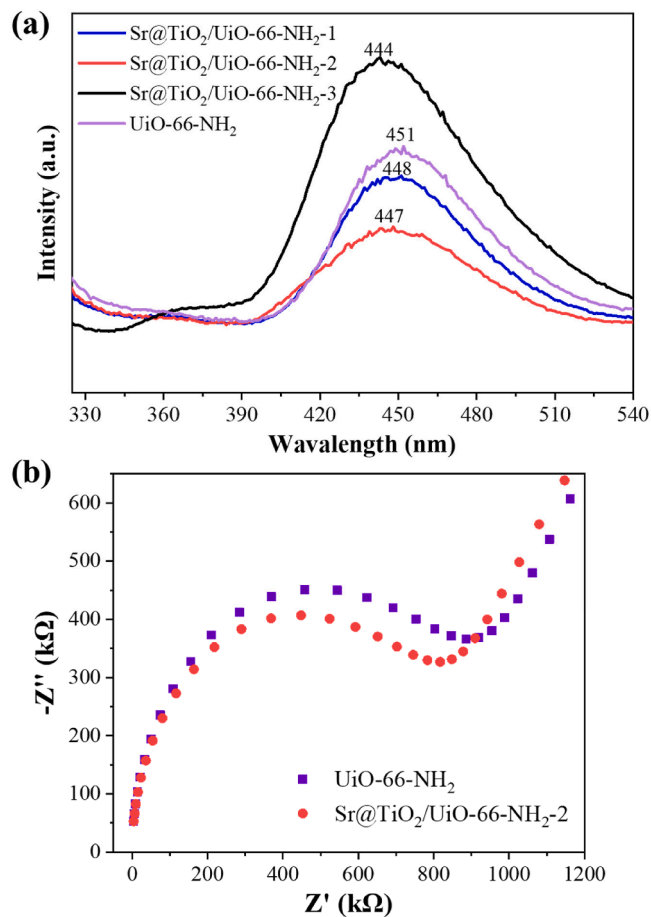


Fig. 9. (a) Photoluminescence (PL) spectra of all synthesized photocatalysts; (b) Electrochemical impedance spectroscopy (EIS) Nyquist plots over the 10⁵–0.01 Hz in the dark of UiO-66-NH₂ and Sr@TiO₂/UiO-66-NH₂-2.

the binding energy positions [37]. Thus, it seems that the introduction of Sr@TiO₂ does not alter the chemical environment of both C and Zr elements. When comparing the N 1s spectra (Fig. 6a), certain changes are observed. The three deconvoluted peaks, assigned to N – C, –NH₂ and –NH₃⁺ [47,53], slightly shift to higher binding energies with the presence of Sr@TiO₂ in the heterostructure, suggesting electron migration from the –NH₂ groups in the MOF to Sr@TiO₂ [54]. Concerning the O 1s spectra (Fig. 6b), UiO-66-NH₂ shows the characteristic peaks of the C = O and Zr – O contributions [48]. The Sr@TiO₂/UiO-66-NH₂-2 heterostructure depicts a more complex spectrum fitted in four peaks, with the addition of the Sr – O and Ti – O contributions due to the presence of Sr@TiO₂ in the heterostructure. Fig. 6c represents the Ti 2p spectrum of Sr@TiO₂/UiO-66-NH₂-2, which can be ascribed to the presence of Ti⁴⁺ in octahedral coordination characteristic of TiO₂ anatase. Finally, Fig. 6d shows the deconvoluted Sr 3d spectrum of Sr@TiO₂/UiO-66-NH₂-2. It shows the contributions of Sr-O, Sr-Sr and Sr-OH [55,56].

3.2. Photocatalytic degradation tests

The photocatalytic performance of Sr@TiO₂/UiO-66-NH₂ heterostructures was evaluated in the removal of ACE under simulated solar light. The adsorption capacity of the photocatalysts was studied in dark prior to light irradiation, being almost negligible after 60 min. Fig. 7a shows that all heterostructures yielded higher ACE conversions than UiO-66-NH₂, achieving the best results with Sr@TiO₂/UiO-66-NH₂-2, which reaches almost complete ACE conversion after 4 h under irradiation. The photocatalytic performance of Sr@TiO₂/UiO-66-NH₂-2 is even better than that described by the SrTiO₃ precursor and the

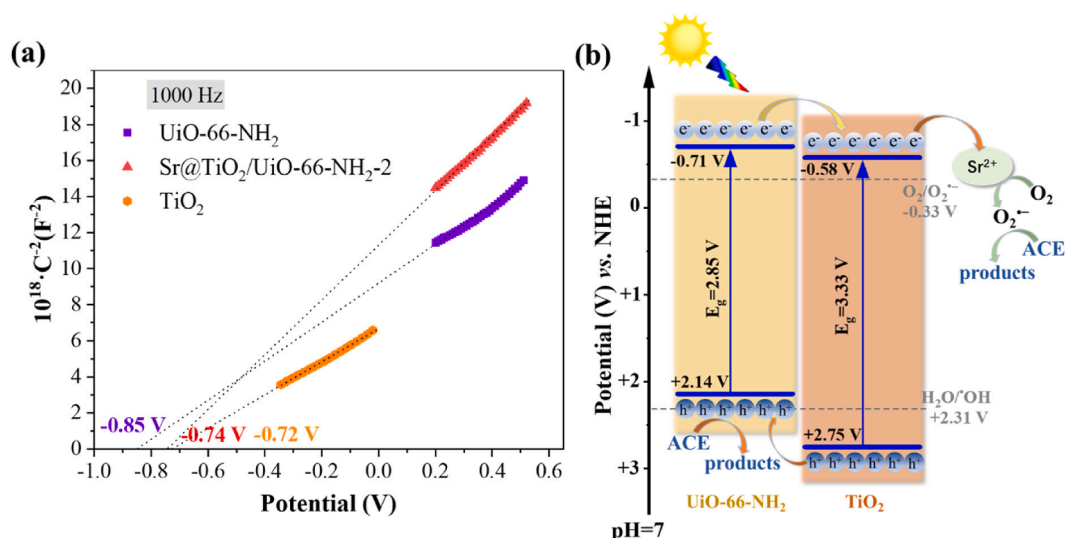


Fig. 10. (a) Mott-Schottky plots of UiO-66-NH₂ and Sr@TiO₂/UiO-66-NH₂-2 at frequencies of 1000 Hz; (b) Proposed charge transfer route in Sr@TiO₂/UiO-66-NH₂-2 heterojunction for the ACE degradation.

synthesized Sr@TiO₂ (Fig. 7c). The pseudo-first-order kinetics more clearly compare the order of photodegradation rates (Fig. 7d). Thus, it seems that there is a synergistic effect between UiO-66-NH₂ and Sr@TiO₂. Regarding the contribution of Sr@TiO₂ loading, it is clear that a more efficient degradation of the pharmaceutical is yielded with the increase of the Sr@TiO₂ amount in the MOF-based heterojunction, being observed at the upper limit with Sr@TiO₂/UiO-66-NH₂-2, probably ascribed to the slight reduction of the bandgap. This effect is also observed when comparing the rate constants, successfully fitted to pseudo-first-order kinetics (Fig. 7b). The *k* value of Sr@TiO₂/UiO-66-NH₂-2 was almost 2-fold higher than that of UiO-66-NH₂ and is also higher than those reported in the literature for ACE degradation with other TiO₂-based heterostructures under identical reaction conditions (Table S2). Considering the outstanding degradation performance of Sr@TiO₂/UiO-66-NH₂-2, this photocatalyst was used in subsequent experiments.

Fig. 8 represents the results of the trapping experiments with different scavengers performed to explore the photocatalytic mechanism of ACE degradation with the heterostructure. The contribution of electrons and $\cdot\text{OH}$ was studied by adding AgNO₃ and 2-propanol, respectively, to the reaction medium [57,58]. A very slight reduction in the degradation profile was observed with both scavengers, which suggests a low contribution of both species (e^- and $\cdot\text{OH}$) in the photodegradation process. A more noticeable effect was observed when using triethanolamine (TEA) and p-benzoquinone (p-BQ) as a scavenger of holes (h^+) and superoxide radicals ($\text{O}_2^{\cdot-}$), respectively. The high decrease in the photocatalytic activity reveals the importance of h^+ and $\text{O}_2^{\cdot-}$ as the main active species during the ACE degradation with Sr@TiO₂/UiO-66-NH₂-2.

The activity of photocatalysts is largely dependent on charge transfer and the ability to separate photogenerated electron-hole pairs. Photoluminescence (PL) spectroscopy, time-resolved fluorescence (TRF) and electrochemical impedance (EIS) spectroscopy were used to characterize the electrochemical behavior of the samples. All heterostructures exhibit similar PL profiles to that of UiO-66-NH₂ (Fig. 9a), but the intensity changes are depending on the Sr@TiO₂ proportion. In general, weaker luminescence intensity implies a lower recombination rate of the photogenerated electron-hole pairs, which would explain the higher activity of the Sr@TiO₂/UiO-66-NH₂-2. Fig. S5 represents the time-resolved fluorescence spectra and summarizes the lifetimes of photogenerated charge carriers for all samples [59]. The longer charge lifetime of Sr@TiO₂/UiO-66-NH₂-2 with respect to UiO-66-NH₂ indicates an

improvement in the charge separation efficiency in the heterostructure. Therefore, it can be inferred that the introduction of an appropriate proportion of Sr@TiO₂ favors the electron-hole pair separation and consequently the photocatalytic activity. The electrochemical impedance spectra shown in Fig. 9b further explores the charge-transfer properties of the Sr@TiO₂/UiO-66-NH₂-2. The smaller radius of the Nyquist curve usually implies a smaller charge-transfer resistance, herein described by the Sr@TiO₂/UiO-66-NH₂-2. Thus, the electrons and holes can be transferred rapidly in this heterostructure yielding a more efficient interface charge-carriers transfer [60]. Concluding, Sr@TiO₂/UiO-66-NH₂-2 described the lowest recombination rate, the longest lifetime of the photogenerated charges and the fastest charge transfer, thus explaining its best photocatalytic performance.

A more comprehensive understanding of the Sr@TiO₂/UiO-66-NH₂-2 performance was acquired by estimating the flat-band potentials and determining the band structure with the Mott-Schottky plots shown in Fig. 10a. The positive slope of the C^{-2} versus the potential plot confirms the n-type semiconductor characteristic of UiO-66-NH₂ and Sr@TiO₂/UiO-66-NH₂-2. The potentials of the flat bands (V_{fb}) estimated by x-intercept and using the Mott-Schottky equation are -0.88 and -0.77 V for UiO-66-NH₂ and Sr@TiO₂/UiO-66-NH₂-2, respectively. For comparison, the flat band of anatase TiO₂ prepared by the solvothermal method [61] was also measured to be -0.75 V. The energy of the conduction band (E_{CB}) at pH = 7 was calculated according to the following equation (where $\Delta V_{(Ag/AgCl; NHE)} = 0.21$ V) [62]:

$$V_{CB} = V_{fb(Ag/AgCl, pH)} + \Delta V_{(Ag/AgCl; NHE)} - 0.059 \cdot (7 - pH)$$

Hence, the V_{CB} of UiO-66-NH₂ and TiO₂ were -0.71 and -0.58 V, respectively. Combining these values with the bandgap ones determined by the Tauc plots (Fig. 5, Table 1) and the bandgap of anatase TiO₂ (3.33 V) [61], the valence band energy of UiO-66-NH₂ and TiO₂ were estimated at +2.14 and +2.75 V, respectively, by using the equation $V_{VB} = V_{CB} + E_g/e$. With these values, the heterojunction bands scheme was proposed (Fig. 10b), describing the characteristic charge transfer route of type II heterojunction [63,64]. Electron and hole pairs were generated by both UiO-66-NH₂ and TiO₂ under irradiation. Photogenerated electrons were then transferred from UiO-66-NH₂ to Sr@TiO₂, where Sr^{2+} acts as an electron trap [42]. Meanwhile, photogenerated holes transferred in the opposite direction (Fig. 10b), directly interact with ACE molecules. In this way, the photogenerated electrons and holes were spatially separated, supporting the low recombination rate, long lifetime of the charges and fast charge transfer previously determined. Since the

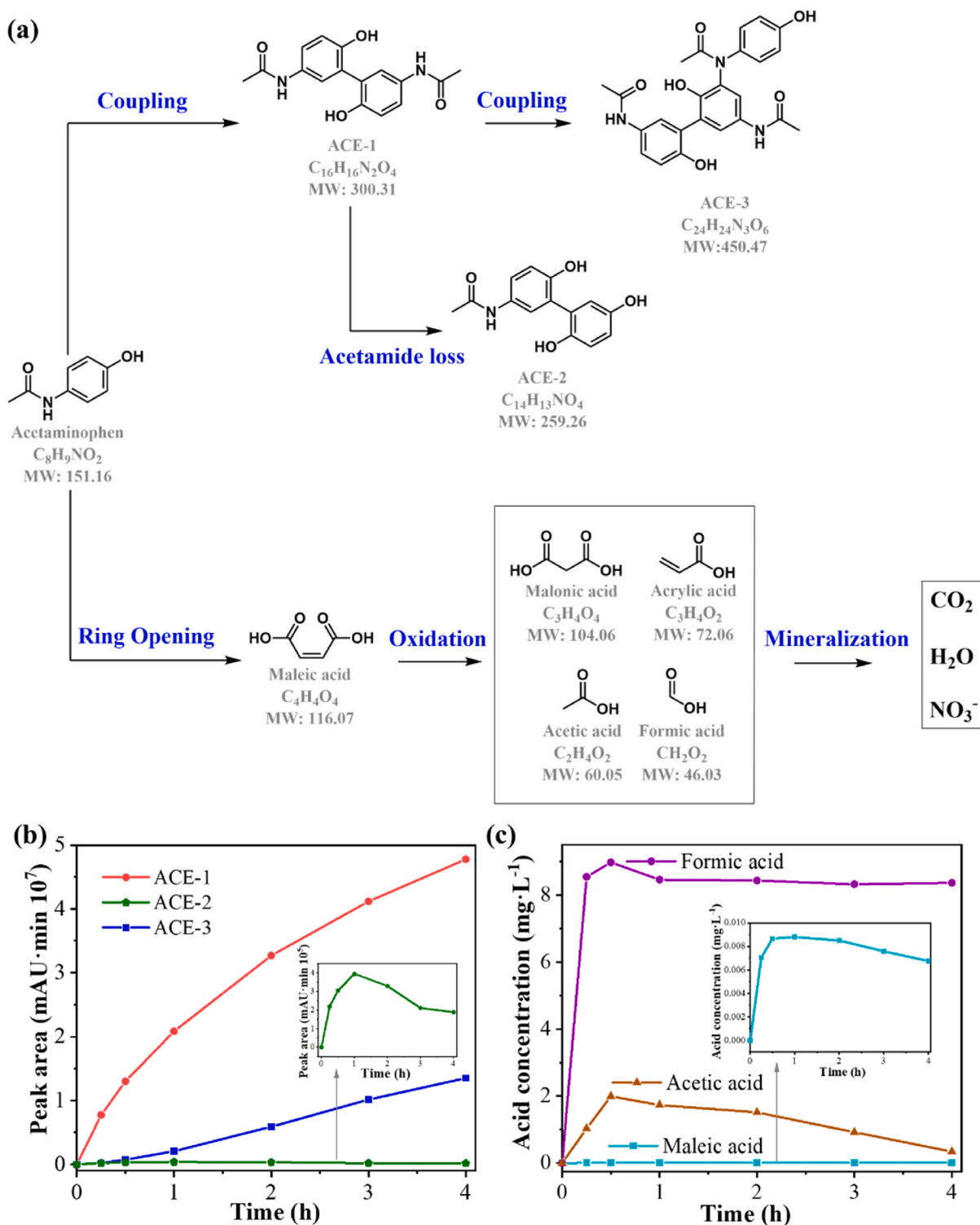


Fig. 11. (a) Proposed photocatalytic pathways, and time-course evolution of (b) major byproducts and (c) short-chain carboxylic acids detected during ACE photodegradation with Sr@TiO₂/UiO-66-NH₂ ([ACE]₀ = 100 mg·L⁻¹; [catalyst] = 250 mg·L⁻¹; Intensity = 600 W·m⁻²).

ECB of both semiconductors remains above the redox potential of superoxide radicals ($E(O_2/O_2^{\bullet-}) = -0.33$ V vs. NHE) [65,66], the generation of $O_2^{\bullet-}$ is allowed, supporting their contribution to ACE degradation previously proved. However, the redox potential of hydroxyl radicals ($E(H_2O/\bullet OH) = +2.31$ V vs. NHE [67]) is not properly positioned with respect to the E_{VB} of the heterojunction, explaining the lower relevance of $\bullet OH$ in the mechanism.

The previous results of TOC analysis show that ACE is partially

mineralized to H_2O and CO_2 during photodegradation, while ACE simultaneously produces a range of intermediate oxidation products. LC/ESI-MS and HPLC were used to identify the chemical formulas of intermediates and transformation products of ACE (Table S3). The proposed ACE pathways by Sr@TiO₂/UiO-66-NH₂-2 heterostructure were depicted in Fig. 11a. The degradation of ACE consists of two main pathways: coupling and ring-opening processes. (i) For coupling, the radical species oxidizes ACE to the single-electron ACE phenoxyl radical,

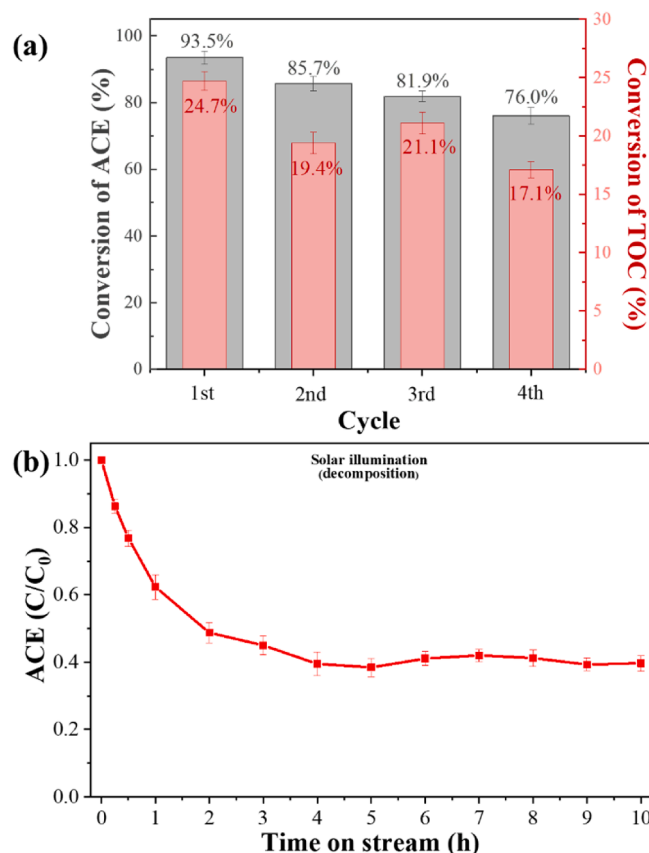


Fig. 12. (a) Conversion of ACE and TOC after four consecutive cycles, and (b) evolution of ACE upon time on stream in a continuous experiment with $\text{Sr@TiO}_2/\text{UiO-66-NH}_2$ ($[\text{ACE}]_0 = 5 \text{ mg}\cdot\text{L}^{-1}$; $[\text{catalyst}] = 250 \text{ mg}\cdot\text{L}^{-1}$; Flow = $0.7 \text{ mL}\cdot\text{min}^{-1}$; Intensity = $600 \text{ W}\cdot\text{m}^{-2}$).

which couples into the dimer ACE-1 (m/z 301.1180) [68]. This byproduct can further lose an acetamide group and undergoes hydroxylation to produce ACE-2 (m/z 260.0916) or continues the coupling process yielding the trimer ACE-3 (m/z 450.1660). The coupling process was previously reported by Peñas-Garzón et al. [69] under similar reaction conditions. From the time-course evolution of byproducts (Fig. 11b), it is worth noting that the content of ACE-1 and ACE-3 increased with time. In contrast, the content of ACE-2 increased up to a maximum after 1 h of reaction, being subsequently partially removed.

The intermediate products of dimer and trimer are lower prone to be further degraded to carbon dioxide and water under the conditions of this work. Therefore, the TOC removal analysis was performed yielding a mineralization rate close to 20%. (ii) In the ring-opening process of ACE, three short-chain carboxylic acids, i.e., maleic, formic, and acetic acids, were detected throughout the experiment. Fig. 11c shows the concentration evolution of these acids over time. In all cases, a maximum concentration was reached after 0.5 h of reaction. After that period, it highlights the decrease in the concentration of maleic and acetic acids. A hint of acrylic acid and malonic acid (below the quantification limit) were detected after 4 h of the degradation process. Eventually, the carboxylic acids would be oxidized by reactive radicals and mineralized into H_2O and CO_2 .

The recycling performance and stability of $\text{Sr@TiO}_2/\text{UiO-66-NH}_2$ were studied by 4-cycle tests (Fig. 12a). The removal efficiency of ACE showed a slight downward trend from 93 to 76%, which may be due to the presence of organic molecules adsorbed at the surface that remained after the washing process between cycles [70]. TOC removal was also evaluated (shown in Fig. 12a) after several cycles, resulting in mineralization close to 25–17% after 4 h of degradation. This could be ascribed to the coupled intermediates identified in the ACE degradation pathways, hindering a further degradation of CO_2 and H_2O . Moreover, the stability of the photocatalytic performance of $\text{Sr@TiO}_2/\text{UiO-66-NH}_2$ was evaluated as a novelty in a continuous flow system (Fig. 12b). A fresh ACE solution was continuously fed to the reactor using the setup schematized in Fig. S1. The steady-state was achieved after 3 h, and the photocatalytic performance remained almost constant throughout the rest of the experiment. This result proved the stability of the photo-degradation when using this heterostructure and its potential for long-term use applications, avoiding the need to recover the photocatalyst from the reaction medium.

After the continuous flow experiment, the $\text{Sr@TiO}_2/\text{UiO-66-NH}_2$ photocatalyst was recovered and characterized by XRD and nitrogen adsorption-desorption at -196°C . The structure and porous texture of $\text{Sr@TiO}_2/\text{UiO-66-NH}_2$ remained unaltered after the long-term experiment (Fig. 13a). A low-significant decrease (less than 5%) of the BET surface area was observed, most likely due to some blockage of micropores with acetaminophen and/or possible degradation byproducts. In addition, the XRD pattern of the used $\text{Sr@TiO}_2/\text{UiO-66-NH}_2$ matches the original pattern well in Fig. 13b, indicating that the heterojunction maintains excellent structural stability. The comparison of the SEM images before and after use (Fig. S6) demonstrated that $\text{Sr@TiO}_2/\text{UiO-66-NH}_2$ photocatalyst suffers no morphological changes during the reaction. Furthermore, EDS mapping (Fig. S7) shows no remarkable variations in the elemental composition and distribution of the main

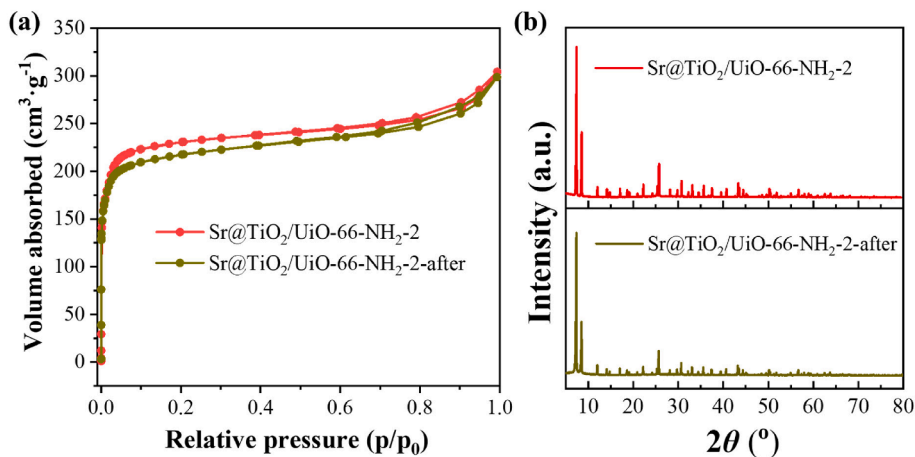


Fig. 13. (a) Nitrogen adsorption-desorption isotherms at -196°C and (b) XRD patterns of $\text{Sr@TiO}_2/\text{UiO-66-NH}_2$ before and after use in continuous flow experiment.

heterojunction components compared to the as-prepared sample (Fig. 3g). This seems to support the outstanding stability of the prepared photocatalyst, and the excellent performance observed in the continuous flow system.

4. Conclusions

Novel Sr@TiO₂/UiO-66-NH₂ heterostructures were constructed by the assembly of Sr@TiO₂ with UiO-66-NH₂ at different ratios using a simple two-step solvothermal method. The improvement in the photocatalytic activity of Sr@TiO₂/UiO-66-NH₂-2 was attributed to a lower charge recombination rate, longer lifetime of the photogenerated charges and faster charge transfer. From radical trapping experiments, it can be inferred that O₂^{•−} and h⁺ played the most significant role in the photocatalytic mechanism. Detailed ACE degradation pathways propose two main oxidation routes, ascribed to coupling and ring opening processes. The analysis of the band positions confirms the formation of a type II heterojunction. Furthermore, 10 h of continuous flow testing demonstrates the outstanding photocatalytic stability of Sr@TiO₂/UiO-66-NH₂-2. This work has positive implications for the photodegradation of contaminants under solar light by heterojunctions based on UiO-66-NH₂ and provides new insights for the potential application of MOF materials in water pollution remediation.

Declaration of Competing Interest

The authors declare that they have no known competing financial interests or personal relationships that could have appeared to influence the work reported in this paper.

Acknowledgements

Financial support from the National State Research Agency of Spain (project number: PID2019-106186RB-I00/AEI/10.13039/501100011033) is gratefully acknowledged. Y.L. Wang acknowledges the financial support provided by China Scholarship Council (CSC No. 201908610198). M. Peñas-Garzón is indebted to Spanish MECD (FPU16/00576 grant). The authors thank S. Zhang from the South China University of Technology (China) for his help with the SEM and TEM images. The authors sincerely acknowledged support from the external services of the Universidad Autónoma de Madrid (SIDI), University of Malaga (SCAI) and Universidad de Zaragoza (Laboratorio de Microscopías Avanzadas).

Appendix A. Supplementary data

Supplementary data to this article can be found online at <https://doi.org/10.1016/j.cej.2022.137229>.

References

- [1] A. Kumar, M. Khan, J. He, I.M.C. Lo, Recent developments and challenges in practical application of visible-light-driven TiO₂-based heterojunctions for PPCP degradation: A critical review, *Water Res.* 170 (2020), 115356, <https://doi.org/10.1016/J.WATRES.2019.115356>.
- [2] Z. Hua, K. Guo, X. Kong, S. Lin, Z. Wu, L. Wang, H. Huang, J. Fang, PPCP degradation and DBP formation in the solar/free chlorine system: Effects of pH and dissolved oxygen, *Water Res.* 150 (2019) 77–85, <https://doi.org/10.1016/J.WATRES.2018.11.041>.
- [3] D.R. Lima, A. Hosseini-Bandegharai, P.S. Thue, E.C. Lima, Y.R.T. de Albuquerque, G.S. dos Reis, C.S. Umpierrez, S.L.P. Dias, H.N. Tran, Efficient acetaminophen removal from water and hospital effluents treatment by activated carbons derived from Brazil nutshells, *Colloids Surfaces A Physicochem. Eng. Asp.* 583 (2019), 123966, <https://doi.org/10.1016/J.COLSURFA.2019.123966>.
- [4] A.J. Ebele, M. Abou-Elwafa Abdallah, S. Harrad, Pharmaceuticals and personal care products (PPCPs) in the freshwater aquatic environment, *Emerg. Contam.* 3 (2017) 1–16, <https://doi.org/10.1016/J.EMCON.2016.12.004>.
- [5] J. Wang, S. Wang, Reactive species in advanced oxidation processes: Formation, identification and reaction mechanism, *Chem. Eng. J.* 401 (2020), 126158, <https://doi.org/10.1016/J.CEJ.2020.126158>.
- [6] J. Wang, R. Zhuan, Degradation of antibiotics by advanced oxidation processes: An overview, *Sci. Total Environ.* 701 (2020), 135023, <https://doi.org/10.1016/J.SCTOTENV.2019.135023>.
- [7] D. Zhu, Q. Zhou, Action and mechanism of semiconductor photocatalysis on degradation of organic pollutants in water treatment: A review, *Environ. Nanotechnol. Monit. Manag.* 12 (2019), 100255, <https://doi.org/10.1016/J.ENMM.2019.100255>.
- [8] C. Belver, J. Bedia, M. Peñas-Garzón, V. Muelas-Ramos, A. Gómez-Avilés, J. J. Rodríguez, Structured photocatalysts for the removal of emerging contaminants under visible or solar light, in: O. Sacco, V. Vaiano (Eds.), *Visible Light Act. Struct. Photocatal. Remov. Emerg. Contam.*, Elsevier, 2020, pp. 41–98, <https://doi.org/10.1016/B978-0-12-818334-2.00003-1>.
- [9] C. Belver, J. Bedia, A. Gómez-Avilés, M. Peñas-Garzón, J.J. Rodríguez, Semiconductor Photocatalysis for Water Purification, in: S. Thomas, D. Pasquini, S.-Y. Leu, D.A. Gopakumar (Eds.), *Nanoscale Mater. Water Purif.*, Elsevier, 2019, pp. 581–651, <https://doi.org/10.1016/B978-0-12-813926-4.00028-8>.
- [10] X. Yu, L. Wang, S.M. Cohen, Photocatalytic metal-organic frameworks for organic transformations, *CrystEngComm* 19 (2017) 4126–4136, <https://doi.org/10.1039/C7CE00398F>.
- [11] H. Dong, G. Zeng, L. Tang, C. Fan, C. Zhang, X. He, Y. He, An overview on limitations of TiO₂-based particles for photocatalytic degradation of organic pollutants and the corresponding countermeasures, *Water Res.* 79 (2015) 128–146, <https://doi.org/10.1016/J.WATRES.2015.04.038>.
- [12] C.B. Ong, L.Y. Ng, A.W. Mohammad, A review of ZnO nanoparticles as solar photocatalysts: Synthesis, mechanisms and applications, *Renew. Sustain. Energy Rev.* 81 (2018) 536–551, <https://doi.org/10.1016/J.RSER.2017.08.020>.
- [13] K.M. Lee, C.W. Lai, K.S. Ngai, J.C. Juan, Recent developments of zinc oxide based photocatalyst in water treatment technology: A review, *Water Res.* 88 (2016) 428–448, <https://doi.org/10.1016/J.WATRES.2015.09.045>.
- [14] S.G. Kumar, K.S.R.K. Rao, Comparison of modification strategies towards enhanced charge carrier separation and photocatalytic degradation activity of metal oxide semiconductors (TiO₂, WO₃ and ZnO), *Appl. Surf. Sci.* 391 (2017) 124–148, <https://doi.org/10.1016/J.APSUSC.2016.07.081>.
- [15] T. Velepini, E. Prabhakaran, K. Pillay, Recent developments in the use of metal oxides for photocatalytic degradation of pharmaceutical pollutants in water—a review, *Mater. Today Chem.* 19 (2021), 100380, <https://doi.org/10.1016/J.MTCH.2020.100380>.
- [16] S. Kanan, M.A. Moyet, R.B. Arthur, H.H. Patterson, Recent advances on TiO₂-based photocatalysts toward the degradation of pesticides and major organic pollutants from water bodies, *https://doi.org/10.1080/01614940.2019.1613323*, 62 (2019) 1–65, <https://doi.org/10.1080/01614940.2019.1613323>.
- [17] R. Koutavarapu, M.R. Tamtam, M.C. Rao, S.G. Peera, J. Shim, Recent progress in transition metal oxide/sulfide quantum dots-based nanocomposites for the removal of toxic organic pollutants, *Chemosphere* 272 (2021), 129849, <https://doi.org/10.1016/J.CHEMOSPHERE.2021.129849>.
- [18] R.R. Solís, J. Bedia, J.J. Rodríguez, C. Belver, A review on alkaline earth metal titanates for applications in photocatalytic water purification, *Chem. Eng. J.* 409 (2021), 128110, <https://doi.org/10.1016/J.CEJ.2020.128110>.
- [19] A. Kumar, A. Kumar, V. Krishnan, Perovskite Oxide Based Materials for Energy and Environment-Oriented Photocatalysis, *ACS Catal.* 10 (2020) 10253–10315, <https://doi.org/10.1021/ACSCATAL.0C02947>.
- [20] C. Byrne, G. Subramanian, S.C. Pillai, Recent advances in photocatalysis for environmental applications, *J. Environ. Chem. Eng.* 6 (2018) 3531–3555, <https://doi.org/10.1016/J.JECC.2017.07.080>.
- [21] M. Sridharan, T. Maiyalagan, Recent progress in Tungsten disulphide based Photocatalyst for Hydrogen Production and Environmental Remediation, *Chem. Eng. J.* 424 (2021), 130393, <https://doi.org/10.1016/J.CEJ.2021.130393>.
- [22] V. Soni, P. Raizada, A. Kumar, V. Hasija, S. Singal, P. Singh, A. Hosseini-Bandegharai, V.K. Thakur, V.-H. Nguyen, Indium sulfide-based photocatalysts for hydrogen production and water cleaning: a review, *Environ. Chem. Lett.* 19 (2) (2021) 1065–1095.
- [23] J. Bedia, V. Muelas-Ramos, M. Peñas-Garzón, A. Gómez-Avilés, J.J. Rodríguez, C. Belver, A Review on the Synthesis and Characterization of Metal Organic Frameworks for Photocatalytic Water Purification, *Catalysis* 9 (2019) 52, <https://doi.org/10.3390/CATAL9010052>.
- [24] S. Gautam, H. Agrawal, M. Thakur, A. Akbari, H. Sharda, R. Kaur, M. Amini, Metal oxides and metal organic frameworks for the photocatalytic degradation: A review, *J. Environ. Chem. Eng.* 8 (3) (2020) 103726.
- [25] Y. Qian, F. Zhang, H. Pang, Y. Qian, H. Pang, F. Zhang, A Review of MOFs and Their Composites-Based Photocatalysts: Synthesis and Applications, *Adv. Funct. Mater.* 31 (2021) 2104231, <https://doi.org/10.1002/ADFM.202104231>.
- [26] Y.C. Wang, X.Y. Liu, X.X. Wang, M.S. Cao, Metal-organic frameworks based photocatalysts: Architecture strategies for efficient solar energy conversion, *Chem. Eng. J.* 419 (2021), 129459, <https://doi.org/10.1016/J.CEJ.2021.129459>.
- [27] A.J. Howarth, Y. Liu, P. Li, Z. Li, T.C. Wang, J.T. Hupp, O.K. Farha, Chemical, thermal and mechanical stabilities of metal-organic frameworks, 2016, pp. 1–15, *Nat. Rev. Mater.* 13 (1) (2016), <https://doi.org/10.1038/natrevmats.2015.18>.
- [28] Q. Wang, Q. Gao, A.M. Al-Enizi, A. Nafady, S. Ma, Recent advances in MOF-based photocatalysis: Environmental remediation under visible light, *Inorg. Chem. Front.* 7 (2020) 300–339, <https://doi.org/10.1039/C9QI01120J>.
- [29] S.A. Younis, E.E. Kwon, M. Qasim, K.H. Kim, T. Kim, D. Kukkar, X. Dou, I. Ali, Metal-organic framework as a photocatalyst: Progress in modulation strategies and environmental/energy applications, *Prog. Energy Combust. Sci.* 81 (2020), 100870, <https://doi.org/10.1016/J.PECS.2020.100870>.
- [30] V. Muelas-Ramos, C. Belver, J.J. Rodríguez, J. Bedia, Synthesis of noble metal-decorated NH₂-MIL-125 titanium MOF for the photocatalytic degradation of

- acetaminophen under solar irradiation, *Sep. Purif. Technol.* 272 (2021), 118896, <https://doi.org/10.1016/J.SEPUR.2021.118896>.
- [31] V. Muelas-Ramos, M.J. Sampaio, C.G. Silva, J. Bedia, J.J. Rodríguez, J.L. Faria, C. Belver, Degradation of diclofenac in water under LED irradiation using combined g-C₃N₄/NH₂-MIL-125 photocatalysts, *J. Hazard. Mater.* 416 (2021), 126199, <https://doi.org/10.1016/J.JHAZMAT.2021.126199>.
- [32] A. Gómez-Avilés, M. Peñas-Garzón, J. Bedia, D.D. Dionysiou, J.J. Rodríguez, C. Belver, Mixed Ti-Zr metal-organic-frameworks for the photodegradation of acetaminophen under solar irradiation, *Appl. Catal. B Environ.* 253 (2019) 253–262, <https://doi.org/10.1016/J.APCATB.2019.04.040>.
- [33] R.R. Solís, A. Gómez-Avilés, C. Belver, J.J. Rodríguez, J. Bedia, Microwave-assisted synthesis of NH₂-MIL-125(Ti) for the solar photocatalytic degradation of aqueous emerging pollutants in batch and continuous tests, *J. Environ. Chem. Eng.* 9 (5) (2021) 106230.
- [34] Y.L. Wang, S. Zhang, Y.F. Zhao, J. Bedia, J.J. Rodríguez, C. Belver, UiO-66-based metal organic frameworks for the photodegradation of acetaminophen under simulated solar irradiation, *J. Environ. Chem. Eng.* 9 (5) (2021) 106087.
- [35] M. Peñas-Garzón, M.J. Sampaio, Y.L. Wang, J. Bedia, J.J. Rodríguez, C. Belver, C. G. Silva, J.L. Faria, Solar photocatalytic degradation of parabens using UiO-66-NH₂, *Sep. Purif. Technol.* 286 (2022) 120467.
- [36] S. Wan, M. Ou, Q. Zhong, X. Wang, Perovskite-type CsPbBr₃ quantum dots/UiO-66 (NH₂)₂ nanojunction as efficient visible-light-driven photocatalyst for Co₂ reduction, *Chem. Eng. J.* 358 (2019) 1287–1295, <https://doi.org/10.1016/J.CEJ.2018.10.120>.
- [37] X. Fang, S. Wu, Y. Wu, W. Yang, Y. Li, J. He, P. Hong, M. Nie, C. Xie, Z. Wu, K. Zhang, L. Kong, J. Liu, High-efficiency adsorption of norfloxacin using octahedral UiO-66-NH₂ nanomaterials: Dynamics, thermodynamics, and mechanisms, *Appl. Surf. Sci.* 518 (2020), 146226, <https://doi.org/10.1016/J.APSUSC.2020.146226>.
- [38] Q. Xu, L. Zhang, B. Cheng, J. Fan, J. Yu, S-Scheme Heterojunction Photocatalyst, *Chem.* 6 (2020) 1543–1559, <https://doi.org/10.1016/J.CHEMPR.2020.06.010>.
- [39] P.A.K. Reddy, P.V.L. Reddy, E. Kwon, K.H. Kim, T. Akter, S. Kalagara, Recent advances in photocatalytic treatment of pollutants in aqueous media, *Environ. Int.* 91 (2016) 94–103, <https://doi.org/10.1016/J.ENVINT.2016.02.012>.
- [40] M. Pelaez, N.T. Nolan, S.C. Pillai, M.K. Seery, P. Falaras, A.G. Kontos, P.S. M. Dunlop, J.W.J. Hamilton, J.A. Byrne, K. O'Shea, M.H. Entezari, D.D. Dionysiou, A review on the visible light active titanium dioxide photocatalysts for environmental applications, *Appl. Catal. B Environ.* 125 (2012) 331–349, <https://doi.org/10.1016/J.APCATB.2012.05.036>.
- [41] Q. Guo, C. Zhou, Z. Ma, Z. Ren, H. Fan, X. Yang, Elementary photocatalytic chemistry on TiO₂ surfaces, *Chem. Soc. Rev.* 45 (2016) 3701–3730, <https://doi.org/10.1039/C5CS00448A>.
- [42] S. Sood, A. Umar, S. Kumar Mehta, A.S.K. Sinha, S.K. Kansal, Efficient photocatalytic degradation of brilliant green using Sr-doped TiO₂ nanoparticles, *Ceram. Int.* 41 (2015) 3533–3540, <https://doi.org/10.1016/J.CERAMINT.2014.11.010>.
- [43] M. Zhou, J. Chen, Y. Zhang, M. Jiang, S. Xu, Q. Liang, Z. Li, Shape-controlled synthesis of golf-like, star-like, urchin-like and flower-like SrTiO₃ for highly efficient photocatalytic degradation and H₂ production, *J. Alloy. Compd.* 817 (2020), 152796, <https://doi.org/10.1016/J.JALLCOM.2019.152796>.
- [44] S. Brunauer, P.H. Emmett, E. Teller, Adsorption of Gases in Multimolecular Layers, *J. Am. Chem. Soc.* 60 (1938) 309–319, <https://doi.org/10.1021/ja01269a023>.
- [45] B.C. Lippens, J.H. de Boer, Studies on pore systems in catalysts: V. The t method, *J. Catal.* 4 (1965) 319–323, [https://doi.org/10.1016/0021-9517\(65\)90307-6](https://doi.org/10.1016/0021-9517(65)90307-6).
- [46] C. Baumanis, D.W. Bahnemann, TiO₂ Thin Film Electrodes: Correlation between Photocatalytic Activity and Electrochemical Properties, *J. Phys. Chem. C* 112 (2008) 19097–19101, <https://doi.org/10.1021/JP807655A>.
- [47] S. Subudhi, L. Paramanik, S. Sultana, S. Mansingh, P. Mohapatra, K. Parida, A type-II interband alignment heterojunction architecture of cobalt titanate integrated UiO-66-NH₂: A visible light mediated photocatalytic approach directed towards Norfloxacin degradation and green energy (Hydrogen) evolution, *J. Colloid Interface Sci.* 568 (2020) 89–105, <https://doi.org/10.1016/J.JCIS.2020.02.043>.
- [48] Z. Yang, X. Tong, J. Feng, S. He, M. Fu, X. Niu, T. Zhang, H. Liang, A. Ding, X. Feng, Flower-like BiOBr/UiO-66-NH₂ nanosphere with improved photocatalytic property for norfloxacin removal, *Chemosphere* 220 (2019) 98–106, <https://doi.org/10.1016/J.CHEMOSPHERE.2018.12.086>.
- [49] X. Liu, H. Li, X. Zhao, Y. Chen, S. Wang, Comparison of the corrosion behavior of copper tubes in formic acid and acetic acid environment, *Mater. Corros.* 72 (2021) 1919–1927, <https://doi.org/10.1002/MACO.202112568>.
- [50] J. Hou, Y. Luan, J. Tang, A.M. Wensley, M. Yang, Y. Lu, Synthesis of UiO-66-NH₂ derived heterogeneous copper (II) catalyst and study of its application in the selective aerobic oxidation of alcohols, *J. Mol. Catal. A: Chem.* 407 (2015) 53–59, <https://doi.org/10.1016/J.MOLCATA.2015.06.018>.
- [51] Q. Liang, S. Cui, C. Liu, S. Xu, C. Yao, Z. Li, Construction of CdS@UiO-66-NH₂ core-shell nanorods for enhanced photocatalytic activity with excellent photostability, *J. Colloid Interface Sci.* 524 (2018) 379–387, <https://doi.org/10.1016/J.JCIS.2018.03.114>.
- [52] Z. Gu, L. Chen, B. Duan, Q. Luo, J. Liu, C. Duan, Synthesis of Au@UiO-66(NH₂)₂ structures by small molecule-assisted nucleation for plasmon-enhanced photocatalytic activity, *Chem. Commun.* 52 (2015) 116–119, <https://doi.org/10.1039/C5CC07042B>.
- [53] H. Zeng, Z. Yu, L. Shao, X. Li, M. Zhu, Y. Liu, X. Feng, X. Zhu, Ag₂CO₃@UiO-66-NH₂ embedding graphene oxide sheets photocatalytic membrane for enhancing the removal performance of Cr(VI) and dyes based on filtration, *Desalination* 491 (2020), 114558, <https://doi.org/10.1016/J.DESAL.2020.114558>.
- [54] P. Hu, R. Wang, Z. Gao, S. Jiang, Z. Zhao, H. Ji, Z. Zhao, Improved interface compatibility of hollow H-Zr_{0.1}Ti_{0.9}O₂ with UiO-66-NH₂ via Zr-Ti bidirectional penetration to boost visible photocatalytic activity for acetaldehyde degradation under high humidity, *Appl. Catal. B Environ.* 296 (2021) 120371.
- [55] J.Y. Baek, L.T. Duy, S.Y. Lee, H. Seo, Aluminum doping for optimization of ultrathin and high-k dielectric layer based on SrTiO₃, *J. Mater. Sci. Technol.* 42 (2020) 28–37, <https://doi.org/10.1016/J.JMST.2019.12.006>.
- [56] Z. Saroukhani, N. Tahmasebi, S.M. Mahdavi, A. Nemati, Effect of working pressure and annealing temperature on microstructure and surface chemical composition of barium strontium titanate films grown by pulsed laser deposition, *Bull. Mater. Sci.* 38 (2015) 1645–1650, <https://doi.org/10.1007/S12034-015-0982-0/TABLES/2>.
- [57] Y.X. Li, X. Wang, C.C. Wang, H. Fu, Y. Liu, P. Wang, C. Zhao, S-TiO₂/UiO-66-NH₂ composite for boosted photocatalytic Cr(VI) reduction and bisphenol A degradation under LED visible light, *J. Hazard. Mater.* 399 (2020), 123085, <https://doi.org/10.1016/J.JHAZMAT.2020.123085>.
- [58] J. Sun, S. Feng, S. Feng, Hydrothermally synthesis of MWCNT/N-TiO₂/UiO-66-NH₂ ternary composite with enhanced photocatalytic performance for ketoprofen, *Inorg. Chem. Commun.* 111 (2020), 107669, <https://doi.org/10.1016/J.INOCHE.2019.107669>.
- [59] L. Yang, J. Huang, L. Shi, L. Cao, Q. Yu, Y. Jie, J. Fei, H. Ouyang, J. Ye, A surface modification resultant thermally oxidized porous g-C₃N₄ with enhanced photocatalytic hydrogen production, *Appl. Catal. B Environ.* 204 (2017) 335–345, <https://doi.org/10.1016/J.APCATB.2016.11.047>.
- [60] M. Zhang, X. Bai, D. Liu, J. Wang, Y. Zhu, Enhanced catalytic activity of potassium-doped graphitic carbon nitride induced by lower valence position, *Appl. Catal. B Environ.* 164 (2015) 77–81.
- [61] M. Peñas-Garzón, A. Gómez-Avilés, J. Bedia, J. Rodríguez, C. Belver, Effect of activating agent on the properties of TiO₂/activated carbon heterostructures for solar photocatalytic degradation of acetaminophen, *Materials (Basel)*. 12 (3) (2019) 378.
- [62] T. Giannakopoulou, I. Papailias, N. Todorova, N. Boukos, Y. Liu, J. Yu, C. Trapalis, Tailoring the energy band gap and edges' potentials of g-C₃N₄/TiO₂ composite photocatalysts for NOx removal, *Chem. Eng. J.* 310 (2017) 571–580, <https://doi.org/10.1016/J.CEJ.2015.12.102>.
- [63] Y. Wang, Q. Wang, X. Zhan, F. Wang, M. Safdar, J. He, Visible light driven type II heterostructures and their enhanced photocatalysis properties: a review, *Nanoscale*. 5 (2013) 8326–8339, <https://doi.org/10.1039/C3NR01577G>.
- [64] G. Di Liberto, S. Tosoni, F. Illas, G. Pacchioni, Nature of SrTiO₃/TiO₂ (anatase) heterostructure from hybrid density functional theory calculations, *J. Chem. Phys.* 152 (18) (2020) 184704.
- [65] Y. Zhang, J. Zhou, Q. Feng, X. Chen, Z. Hu, Visible light photocatalytic degradation of MB using UiO-66/g-C₃N₄ heterojunction nanocatalyst, *Chemosphere* 212 (2018) 523–532, <https://doi.org/10.1016/J.CHEMOSPHERE.2018.08.117>.
- [66] D. Jiang, P. Xu, H. Wang, G. Zeng, D. Huang, M. Chen, C. Lai, C. Zhang, J. Wan, W. Xue, Strategies to improve metal organic frameworks photocatalyst's performance for degradation of organic pollutants, *Coord. Chem. Rev.* 376 (2018) 449–466, <https://doi.org/10.1016/J.CCR.2018.08.005>.
- [67] W.H. Koppenol, D.M. Stanbury, P.L. Bounds, Electrode potentials of partially reduced oxygen species, from dioxygen to water, *Free Radic. Biol. Med.* 49 (2010) 317–322, <https://doi.org/10.1016/J.FREERADBIOMED.2010.04.011>.
- [68] J. Qi, J. Liu, F. Sun, T. Huang, J. Duan, W. Liu, High active amorphous Co(OH)₂ nanocages as peroxymonosulfate activator for boosting acetaminophen degradation and DFT calculation, *Chinese Chem. Lett.* 32 (2021) 1814–1818, <https://doi.org/10.1016/J.CCLET.2020.11.026>.
- [69] M. Peñas-Garzón, A. Gómez-Avilés, C. Belver, J.J. Rodríguez, J. Bedia, Degradation pathways of emerging contaminants using TiO₂-activated carbon heterostructures in aqueous solution under simulated solar light, *Chem. Eng. J.* 392 (2020), 124867, <https://doi.org/10.1016/J.CEJ.2020.124867>.
- [70] W. Cao, Y. Zhang, Z. Shi, T. Liu, X. Song, L. Zhang, P. Keung Wong, Z. Chen, Boosting the adsorption and photocatalytic activity of carbon fiber/MoS₂-based weavable photocatalyst by decorating UiO-66-NH₂ nanoparticles, *Chem. Eng. J.* 417 (2021), 128112, <https://doi.org/10.1016/J.CEJ.2020.128112>.